ADVANCED FUNCTIONAL MATERIALS
www.afm-journal.de

Continuously-Tunable and Ultrawide-Range Thermal Regulator Based on Superaligned Carbon Nanotube Aerogels for Dynamic Thermal Management of Batteries and Buildings

Wei Yu, Wenhua Dai, Zixin Hong, Guoxian Li, Ziying Wang, Chuizhou Meng, Jiaping Wang,* Changhong Liu,* Shijie Guo, and Shoushan Fan*

Efficient heat transfer control is highly demanded for dynamic thermal management of equipment and buildings especially when the environmental temperature dramatically changes. Thermal switches, the current approach of heat transfer control, suffer from the issues of low switching ratios below eight and sharp state transition between "on" and "off". Herein, a continuously-tuned thermal regulator with an ultrahigh thermal-conductivity change ratio of 43 based on superaligned carbon nanotube aerogel is reported, which works on the regulation of both thermal interfacial resistance and conduction pathways by compressive deformation-induced microstructure evolution. This thermal regulator can stabilize the device temperature at 25 °C when the environmental temperature varies by 7 and 11 °C under the natural convection and forced convection conditions, respectively. Toward practical application, the thermal regulator with flexibility is wrapped around a cylindrical lithium-ion battery to control the operation temperature within the optimal range of 20–40 °C for enhanced discharging performance even at an environmental temperature of −20 °C. Besides, by combining the thermal regulator with radiative cooling film, the house model temperature can be lowered by 2.7 °C during daytime and raised by 1.1 °C during nighttime compared with the bare one. This efficient thermal regulation approach offers an effective solution for practical thermal management.

1. Introduction

Nowadays, ≈90% of global energy utilization is closely related to the generation and manipulation of heat.[1] Consequently, efficient heat transfer control is crucial to improving energy efficiency and mitigating global warming. Thermal switches,[2,3] the devices that can control the heat flux in a real-time mode by using an external stimulus, have great potential for active dynamic thermal management when the ambient or operating conditions dramatically change, such as batteries,[4,5] buildings,[6,7] and spacecraft.[8] Since the thermal conduction relies on the thermal carrier transport behavior,[9] many researchers focus on the development of thermal switches by modulating materials at the molecular or atomic scale, such as phase transition (e.g., solid–liquid,[10,11] metal-insulator,[12] and semiconductor-metal phase transition[13]), and electrochemical intercalation.[3,14,15] However, the limited number of available phase transition states or the inherent rigidity of crystalline frameworks lead to a discontinuous and narrow-range regulation.[14] The low thermal-conductivity change ratios and sharp state transition between "on" and "off" severely limit their practical applications. Therefore, thermal regulators, which is able to tune the thermal conductance continuously and possess significantly larger change ratios are urgently needed to be developed.

Past attempts show that material selection and effective regulation methods are vital for thermal regulation.[14] Carbon nanotube (CNT) materials could vary by five orders of magnitude from the thermal superconductor of single CNT (≈3000 W m^{-1} K^{-1})[16] to the thermal super-insulator of CNT aerogels (≈0.02 W m^{-1} K^{-1}),[17] demonstrating its great potential for thermal conduction modulation. In our previous work, the thermal conductivity of CNT films has been successfully tuned with a modulation ratio of four by changing the stacking angles.[18] However, dynamic and continuous thermal regulation has not yet been achieved because the stacking angle remains fixed once

W. Yu, W. Dai, G. Li, Z. Wang, C. Meng, S. Guo
State Key Laboratory for Reliability and Intelligence of Electrical Equipment
Engineering Research Center of Ministry of Education for Intelligent Rehabilitation Device and Detection Technology
Hebei Key Laboratory of Smart Sensing and Human-Robot Interaction
School of Mechanical Engineering
Hebei University of Technology
Tianjin 300401, China
E-mail: 2018108@hebut.edu.cn
Z. Hong, J. Wang, C. Liu, S. Fan
Tsinghua-Foxconn Nanotechnology Research Center and Department of Physics
Tsinghua University
Beijing 100084, China
E-mail: jpwang@tsinghua.edu.cn; chliu@tsinghua.edu.cn
The ORCID identification number(s) for the author(s) of this article can be found under https://doi.org/10.1002/adfm.202314021

DOI: 10.1002/adfm.202314021

determined.[18] Mechanical deformation,[4,19] the much simpler approach compared to the strong magnetic field and ultralow temperature,[20] is promising to solve the above-mentioned issue. It has been proven effective in adjusting the thermal conduction of carbon nanomaterials.[4] Zeng and co-workers tuned the thermal transport in polycrystalline graphene by strain engineering.[21] However, the changes in the thermal transport pathways are limited by the small deformation (1%), and the modulation of thermal conduction mainly arises from variations in grain boundary phonon-scattering behavior, resulting in a very small modulation ratio of 1.4. Although the carbon/polymer composites possess good compressive deformation capability (50–85%), which can more effectively adjust heat conduction pathways,[4,22] the large interfacial thermal resistance originating from the acoustic mismatch between two kinds of materials of carbon and polymer still hinders the modulation property.[23,24] These results demonstrate that simultaneous control of both the heat conduction pathways and the interfacial thermal resistance in an effective way is vital for achieving a broad range of modulation, but still remains a challenge.

In this work, we develop a continuously tuned and ultrawide-range thermal regulator with an extremely high thermal-conductivity change ratio ($r \approx 43$) based on the superaligned carbon nanotube (SACNT) aerogel, which works on the principle of compressive deformation-induced thermal conduction change. The excellent heat transfer control originates from the regulation of both thermal interfacial resistance and conductive pathways by the microstructure evolution of the highly porous SACNT network with a large compressive deformation of up to 90%. Different from the conventional thermal switch with only "on" and "off" state (**Figure 1a**), this new type of thermal regulator has continuously adjustable thermal resistance capability (Figure 1b) and can be used to stabilize the temperature of target device (Figure 1c). The experiments show that the device temperature can be maintained at 25 °C even when the ambient temperature varies by a large difference of 7 and 11 °C under the natural convection and the forced convection conditions, respectively. Benefitting from the outstanding flexibility, the thermal regulator can be wrapped around a cylindrical lithium-ion battery to actively control the operation temperature within the optimal range of 20–40 °C for enhanced discharging performance even when the environmental temperature is −20 °C. Meanwhile, by combining the thermal regulator with radiative cooling film (Figure 1d), the temperature of a house model can be actively lowered by 2.7 °C during daytime and raised by 1.1 °C during nighttime compared with the bare house model. The developed thermal regulator device with high mechanical flexibility and excellent thermal transfer control ability provides an efficient and smart way for effective thermal management in dynamic temperature-changing environments.

2. Results and Discussion

2.1. Fabrication and Characteristics of the Thermal Regulator

Different from ordinary CNTs, the SACNT arrays we fabricated are well-aligned and have very clean surfaces which lead to strong van der Waals interaction between CNTs.[25–27] Benefiting from this, the self-supported CNT aerogels can be fabricated by simple ultrasonication and freeze-drying procedures, without using any organic binder or templates.[26] However, we found that to obtain a sponge with ordinary CNT, additional organic binders are needed to glue CNT together, potentially impacting both thermal and chemical stability.[26] Therefore, the CNT aerogels made from SACNT arrays were named SACNT aerogels to distinguish them from aerogels made from ordinary CNTs according to our previous report.[26] To increase the mechanical properties, the carbon deposition process was followed as described in Figure S1 (Supporting Information). The SACNT aerogels exhibit an ultra-low density of 1.3 mg cm^{-3} and high flexibility (Figure 1e). A similar crystallinity is observed before and after carbon deposition (Figure S2, Supporting Information). Due to the CNT–CNT welding network, the self-supporting SACNT aerogels have superior mechanical properties and can be laser-cut into various shapes (Figure 1f). Especially, aerogels possess extraordinary elasticity, which is highly necessary for their practical application. Almost full volume and shape recovery is observed at compressive strain up to 90% even after 3000 compressive cycles (Figure 1g). This impressive fatigue resistance can not only be attributed to the strong van der Waals force between CNTs,[26] but also to the welded junctions reinforced by the deposited graphite layer (Figure S3, Supporting Information).[28,29] The microstructure evolution of SACNT aerogels was characterized during the compressive process as shown in Figure 1h–j. The original SACNT aerogel exhibits a hierarchical porous structure formed by the random-distributed CNT bundles (Figure 1h). For the aerogel under 40% compressive strain, a noticeable reduction in pore size can be observed (Figure 1i). When it is further compressed to 90%, the aerogel becomes an ordered stacking structure which is considered as the fully compressed state (Figure 1j). This dramatic structure evolution would have a significant effect on the thermal conductive pathways and the contact resistance between CNTs, and the detailed studies of this tunable thermal transport are presented in the following sections.

2.2. Dynamically Tunable Thermal Transport in the Thermal Regulator

The thermal conductivity of SACNT aerogel (**Figure 2a**) under different compressive strains was measured by the hot-disk method according to the previous report.[30] A minor change of thermal conductivity is observed when the strain is <40%, because the high volume fraction of air severely limits the effective contact between CNTs. As the strain increases from 50 to 90%, the thermal conductivity of SACNT aerogel dramatically gets larger because many more tubes contact together to result in an increased density of effective conductive pathways. The aerogel's thermal conductivity changes from 0.03 W m^{-1} K^{-1} at 0% strain to 1.29 W m^{-1} K^{-1} at 90% strain and yields a modulation ratio of ≈43, which surpasses the results reported in previous studies.[10,11,31–35] However, this significant change is much smaller than the results calculated based on effective medium theory (Figure S4, Supporting Information), where the thermal conductivity increases with mass density and reaches as high as ≈3.00 W m^{-1} K^{-1} at 90% compressive strain. This difference can be attributed to that the contact thermal resistance between tubes is neglected in the effective medium theory.[22] Additionally, this difference can also be attributed to that we did not consider the reduction in

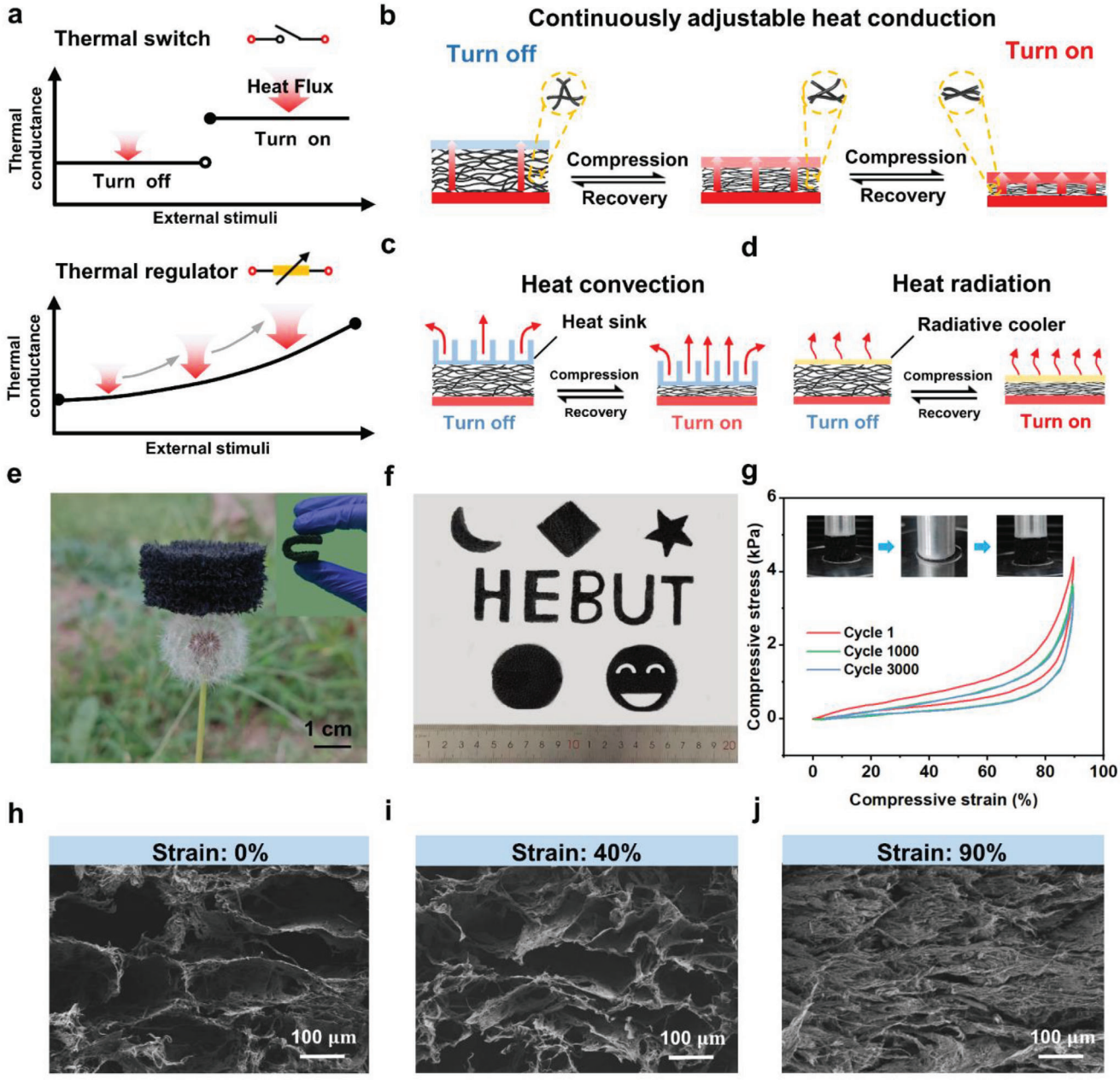

Figure 1. Design and characterization of the thermal regulator. a) Schematic diagrams illustrating the difference between the thermal switch and the thermal regulator. b) Schematic diagram illustrating the continuously adjustable heat conduction of the SACNT aerogel-based regulator upon mechanical deformation. c,d) Schematic diagrams illustrating the heat transfer control of SACNT aerogel under the heat convection condition (c) and radiation condition (d). e) Photograph showing the low mass density and high mechanical flexibility of SACNT aerogel. f) Photographs of SACNT aerogels with different shapes and sizes. g) Stress–strain curves of SACNT aerogel upon cyclic compression. h–j) SEM images showing the cross-sectional view of SACNT aerogel under different strains of 0% (h), 40% (i), and 90% (j).

thermal conductivity of CNTs along the vertical direction due to the planar alignment of CNTs during compression. The total thermal resistance (R_{total}) of phonon transport in CNT aerogel stems from the thermal resistance of the tube (R_{tube}) and tube–tube contact ($R_{contact}$).[22] Based on this, the calculated results in Figure 2b show that $R_{contact}$ decreases with compressive strain, and its contribution to the total thermal resistance reduces from 90 to 54% (see Section S3, Supporting Information for calculation details). This indicates that thermal contact resistance modulated by compressive strain plays a great role in thermal regulation.

However, solely relying on microstructure changes is still insufficient to achieve a wide-range thermal conduction modulation. As shown in Figure 2c, melamine sponge, as a kind of great insulator, has similar thermal conductivity (0.03 W m^{-1} K^{-1}) to SACNT aerogel at the initial state. Interestingly, the thermal conductivity under the compressive strain of 90% is 0.06 W

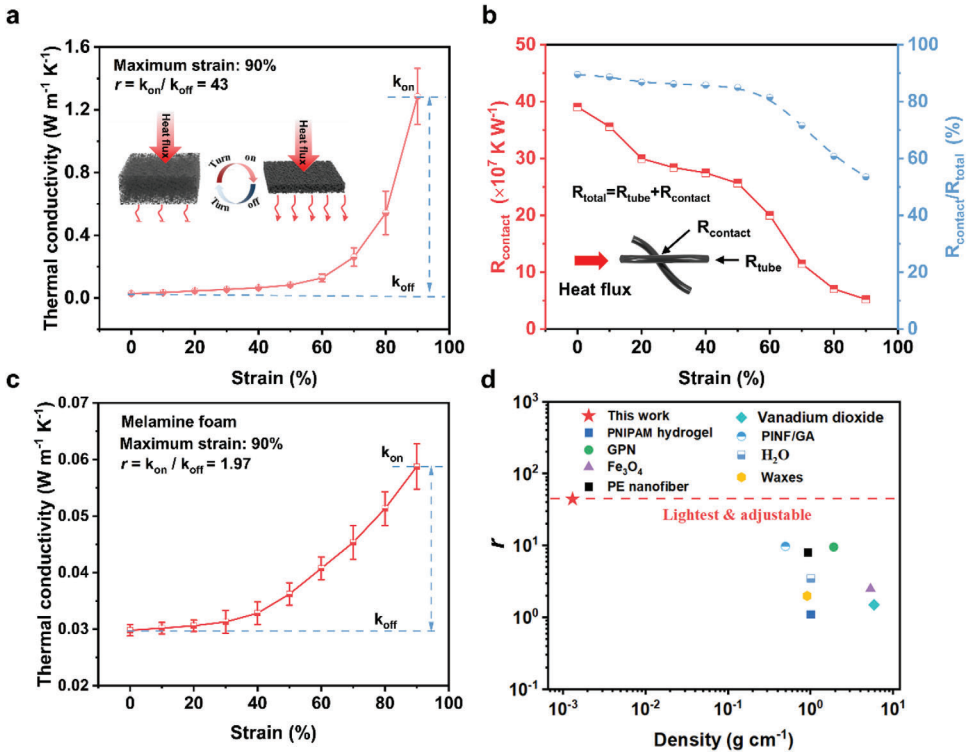

Figure 2. Thermal transport in the thermal regulator. a) Thermal conductivity of SACNT aerogel under different compressive strains. b) Changes of the tube–tube contact resistance and the ratio of the tube–tube contact thermal resistance to the total thermal resistance under different compressive strains. c) Thermal conductivity of the pristine melamine foam under different compressive strains. d) Comparison of thermal-conductivity change ratio and mass density between the thermal regulator developed in this work and those reported in literature.[10,11,31–35]

m^{-1} K^{-1}, leading to a much smaller thermal-conductivity change ratio ($r \approx 2$) than SACNT aerogel. This indicates that the low thermal conductive ability of the polymer severely hinders heat transfer,[36] although thermal pathways and contact resistance increase under compression. Therefore, the superior thermal conduct property of CNTs, combined with the dramatic changes in the conductive path and contact resistance, together enable the continuously tunable wide-range thermal conduction. Compared with the thermal switches based on phase-change material (PCM) and thermal regulators based on carbon composites in previous reports,[10,11,31–35] our thermal regulator not only has a much higher thermal-conductivity change ratio but also a lower density (Figure 2d).

2.3. Heat Transfer Control Under the Natural and Forced Convection Conditions

Since the convective heat transfer is influenced by the temperature difference between the fluid and solid, modulating the heat sink temperature by the thermal regulator can effectively control convective heat dissipation, thereby achieving device thermal management. To evaluate the performance of our thermal regulator, the experiment to control natural and forced convective heat transfer under different ambient temperatures was conducted (see Section S4, Supporting Information for experimental details). **Figure** 3a shows the modulated device temperature, T_d, at a fixed heat of 3670 W m^{-2} in the natural convection conditions. Here, T_d is approximated as the temperature of the upper surface of the copper. It shows that T_d almost linearly increased with the environment temperature for the SACNT aerogel with fixed thickness and has a tunable temperature window of ≈7 °C at fixed ambient temperature. For example, T_d goes from 44 to 37 °C when the thermal regulator switches from "off" to "on" at an ambient temperature of 20 °C. Despite the fluctuations in environmental temperature, T_d can still be maintained with the thermal regulator. Just like the blue shadow displayed in Figure 3a, if the optimal operating temperature range for the device is from 25 to 30 °C, the environmental temperature can vary from 0.8 to 12.8 °C, indicating an excellent thermal management capacity. Similarly, T_d can also be effectively regulated when the heat flux changes at fixed ambient temperature as shown in Figure 3b. The tunable window of T_d increases with the heat flux, reaching the maximum of 12.5 °C at the heat flux of 5090 W m^{-2}. To explain this great heat transfer control capability, a simulation based on finite element analysis was developed. It shows that with the thermal regulator at the "on" state, the system reaches a significantly lower temperature distribution compared to that when the regulator is at the "off" state (Insert of Figure 3c), which is consistent with the experimental results. This phenomenon can be attributed to the significant difference in heat convection (Figure 3c), where the ratio of convective heat dissipated by the heat sink to total input heat (q_{sink}/q_{in}) increases from 50.5 to 85.4% when the thermal regulator tunes from "off" to "on" state.

The performance of the thermal regulator under the forced convection condition was further explored as shown in Figure 3d.

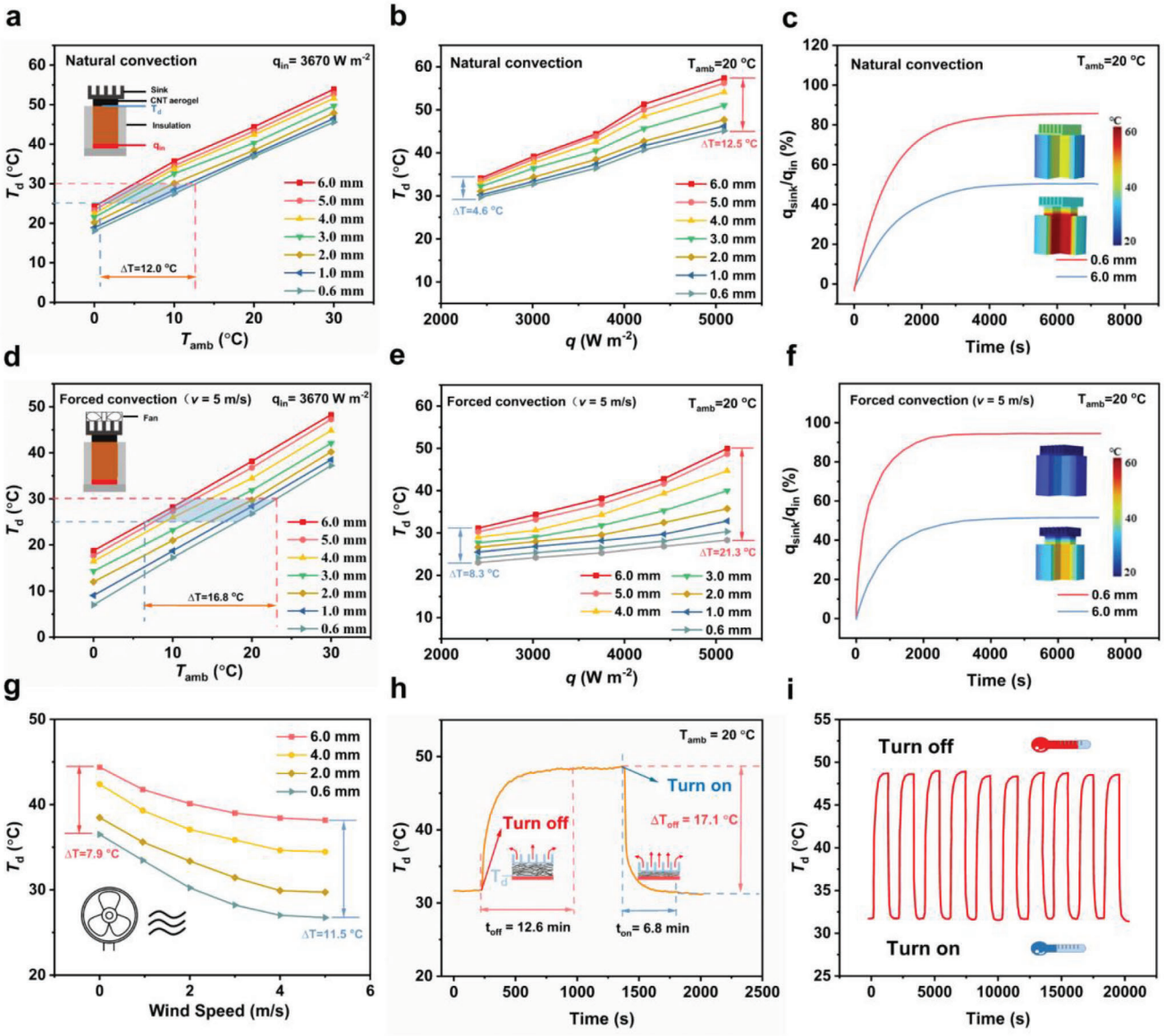

Figure 3. Heat transfer control of the thermal regulator under natural and forced convection conditions. a–c) Under the natural convection condition, the thermal management capability of the SACNT aerogel at different ambient temperatures (a) and at different heat flux (b) as well as the ratio (c) of the heat dissipated by convection of the heat sink to the total input heat based on finite element simulation (insert: temperature distribution of the setup at equilibrium with the thermal regulator at the "on" and "off" state). d–f) Under the forced convection condition, the thermal management capability of SACNT aerogel at different ambient temperatures (d) and at different heat flux (e) as well as the ratio (f) of the heat dissipated by convection of heat sink to the total input heat based on finite element simulation (insert: temperature distribution of the setup at equilibrium with thermal regulator at the "on" and "off" state). g) Thermal management of SACNT aerogel under different wind speeds. h) Transient temperature response of the system during one compression cycle. i) Cycling performance of the thermal regulator.

Compared to natural convection, a more outstanding thermal management capacity was observed. The adjustable temperature window gets larger from ≈7 °C under natural convection to ≈11 °C. To maintain the device temperature in the range of 25–30 °C, the ambient temperature can vary by 16.8 °C (blue shadow in Figure 3d) through changing the thickness of SACNT aerogel. Besides, the tunable window of T_d at the heat flux of 5090 W m^{-2}can expand to 21.3 °C, which is much larger than that under natural convection condition (12.5 °C). The simulated results (Figure 3c,f) demonstrate that when the thermal regulator is at the "off" state, the convective heat dissipation from the heat sink is approximately the same for natural convection and forced convection (q_{sink}/q_{in}≈51%). However, when the thermal regulator is at the "on" state, convective heat dissipation under forced convection (q_{sink}/q_{in}≈94.4%) is significantly greater than that under natural convection (q_{sink}/q_{in}≈85.4%). This phenomenon indicates that the dynamic thermal management performance is positively correlated with the heat dissipation capacity of the heat sink, which can be confirmed by the increasing adjustable temperature window with larger wind speed as displayed in Figure 3g.

Furthermore, response time and cycling stability were investigated for the practical application of our thermal regulator. As shown in Figure 3h, it takes 12.6 min to transition from the temperature-equilibrium state with fully compressed aerogel ("on" state) to the steady state with uncompressed aerogel ("off" state), resulting in a device temperature increase of 17.1 °C. A shorter response time of 6.8 min is observed when the regulator tunes from "off" to "on" state, due to the smaller thermal resistance of the fully compressed SACNT aerogel.[4] This much shorter response than that of thermal switches based on phase change materials would be helpful for their practical applications in preventing thermal runaway or system damage.[11,37] Moreover, Figure 3i illustrates that the thermal regulator has excellent cycling stability, where the device temperature difference when the regulator is at the "on" and "off" state can be maintained at 16.9 °C during the cycles. This excellent cycling performance can be attributed to the great stability of SACNT aerogels thermal-conductivity change performance (Figure S7, Supporting Information).

2.4. Thermal Management of Li-Ion Battery for Optimal Operation Temperature

Current commercial Li-ion Batteries (LIBs) suffer from poor performance at low temperature and safety issues at high temperature, especially for high-rate operation.[38] The commonly used thermal management methods, such as air-based, liquid-based, and PCM-based approaches, only have one single function of cooling the battery. Additional heat-insulating or heating devices are needed to elevate battery temperature when the battery undergoes reduced capacity and efficiency in the cold environment.[39,40] The tunable heat transfer of our thermal regulator is promising to mitigate the above problems by meeting the opposite demands of heat dissipation and heat insulation in different operating and ambient conditions. To prove this, the performance of the thermal regulator in the thermal management of commercial LIBs (18650–3.6 V/2.5Ah) at high discharging rates was further investigated. The setup is illustrated in **Figure 4**a, and more details can be found in Section S5, Supporting Information. SACNT aerogel with excellent flexibility is wrapped around the cylindrical battery, and its compressive strain is controlled by the copper foil. When the LIB undergoes reduced capacity and efficiency at low temperatures (<15 °C),[41] the thermal regulator can be tuned to "off" state by loosening the copper foil to block the heat dissipation (left, Figure 4b). In contrast, the thermal regulator can turn into "on" state by fastening the copper foil to keep the battery from overheating in hot temperatures, especially at high-rate operation (right, Figure 4b). To evaluate the dynamic thermal management of the thermal regulator in a real operating environment, the system is tested in an environmental chamber with tunable temperature. Figure 4c shows the temperature changes of LIBs during the 4C-rate discharge process at an environment temperature of −20 °C. The temperature of LIB with uncompressed SACNT aerogel ("off" state) quickly rises to ≈26 °C by preventing the leakage of the battery's self-generated heat, while both bare battery and battery with fully compressed aerogel ("on" state) exhibit much lower temperatures (<0 °C). As a result, the usable capacity of the battery with uncompressed SACNT aerogel increased by 34% compared with the bare battery (Figure 4d). Besides, the battery with the thermal regulator at "off" state cools down significantly more slowly than bare battery as shown in Figure 4e. It takes ≈50 min for the battery temperature to drop back to the ambient environment, which is considerably helpful for short-interval cycling operations, such as the electric vehicle drive involving brief stops in winter.

However, the superior heat insulation property of the thermal regulator at the "off" state is inappropriate in a hot environment. In this situation, the thermal regulator can be tuned to the "on" state to cool down the battery. To further evaluate the thermal management performance, the 4C-rate discharge performance of batteries with all three thermal management strategies was explored in the hot ambient (40 °C). As shown in Figure 4f, the battery with fully-compressed aerogel ("on" state) exhibits a much lower temperature (<51 °C) than that with uncompressed aerogel ("off" state), whose temperature increases by 25 °C to the unsafe level of 65.3 °C (the alert temperature is 60 °C according to the instruction manual). Besides, the temperature with the thermal regulator at the "on" state is slightly smaller compared with the bare battery, due to the higher emissivity of graphene-coated Cu foil. Although these batteries exhibit similar discharge capacity (Figure 4g), the one with fully-compressed aerogel would discharge 25.5% more capacity than the one with uncompressed aerogel if the discharge process is paused once the battery temperature exceeds the alert temperature for the safety running.

Dynamic thermal management of the battery by the thermal regulator is highly desired in complex operating and environmental conditions. For example, when the battery discharges at a high rate in a cold environment, the battery temperature is desirable to rapidly increase to the optimal operation range (20–40 °C, according to the instruction manual) while remaining below the alert temperature. Our thermal regulator provides an ideal thermal management approach for this purpose. As shown in Figure 4h, the LIB with uncompressed ("off" state) reaches the optimal operating temperature range 250 s earlier than the bare battery. However, the battery temperature rises sharply to 50.7 °C, exceeding the optimal temperature range within 226 s. This high temperature would accelerate battery degradation and thermal runaway.[42] Therefore, we developed a dynamic thermal regulation strategy, where the thermal regulator is at the "off" state to block the heat dissipation at the beginning, and switched to "on" state to prevent further rapid heating once it reaches the optimal temperature. Benefiting from the wide-range adjustable heat transfer, the battery with the dynamic thermal regulation operates for a longer duration within the optimal temperature range than the other two batteries, leading to the best discharging performance (Figure 4i). Besides, the detailed temperature-rising process captured by the infrared camera (Figure 4j; Video S1, Supporting Information) also demonstrates the excellent thermal management which would help improve battery efficiency and lifespan.

2.5. Thermal Management of House Model for Comfortable Living Temperature

Radiative cooling (RC) which cools a surface by radiating heat to the cold outer space through the transparent atmospheric win-

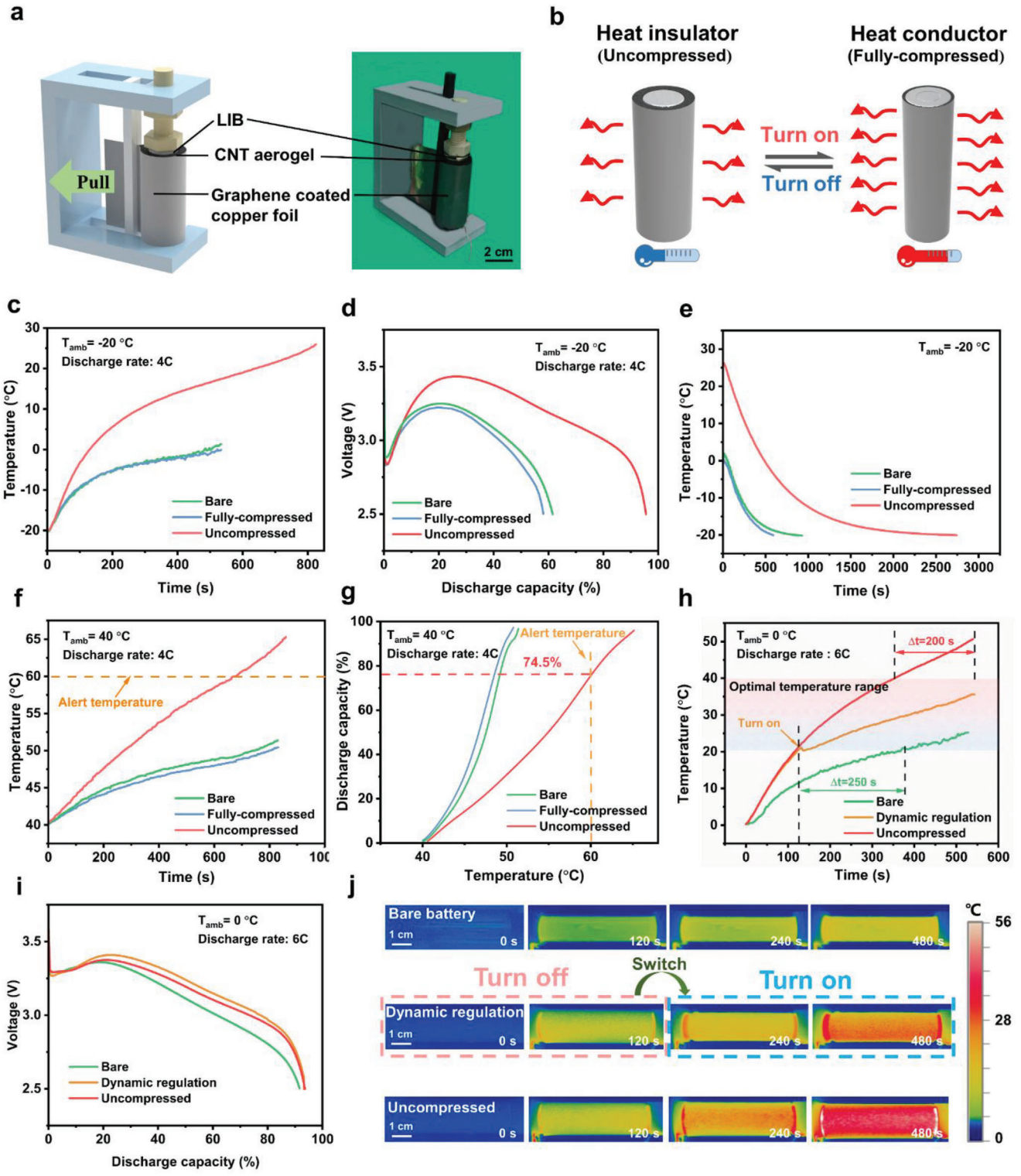

Figure 4. Dynamic thermal management of the commercial LIB. a) Schematic diagram and photograph showing the setup of the battery thermal management experiment. b) Schematic diagram illustrating the working principle of the battery thermal management by the thermal regulator. c–e) At the extremely low ambient temperature of −20 °C, the temperature rise (c) and the discharge capacity (d) of the batteries during the 4C-rate discharge process, and the battery temperature changes after the 4C-rate discharge (e). f,g) At the elevated ambient temperature of 40 °C, the temperature rise (f) and the discharge capacity (g) of the batteries during the 4C-rate discharge process. h–j) At the low ambient temperature of 0 °C, the temperature rise (h), the discharge capacity (i), and the infrared images (j) of the batteries during the 6C-rate discharge process.

dow (8–13 μm) has been extensively studied for its great potential applications in building cooling.[43,44] However, the radiative cooling property is undesirable for the building in a cold environment.[6,7] We proposed an efficient heat radiation control approach based on the thermal regulator since the radiative heat is dependent on the object's surface temperature according to the Stefan-Boltzmann law. As shown in **Figure 5**a, the thermal management device is composed of RC film and thermal regulator and is labeled as RCTR. Here, the Poly(vinylidene fluoride-co-hexafluoropropylene) (PVDF-HFP) film prepared by electrospinning is used as RC film, and it possesses high reflectivity (≈91%) in the solar spectrum and high emissivity (≈0.9) as shown in Figure S10 (Supporting Information). The radiative performance can be tuned by compressing the SACNT aerogel to meet the different heat transfer requirements in the dynamic environment. To evaluate the thermal management performance, an outdoor experiment was conducted via the setup in Figure 5b (see more details in Section S6, Supporting Information). In Figure 5c, it is observed that RCTR at "on" state lowers the temperature by 4.1 and 10.6 °C than the ambient and the sample with RCTR at "off" state at the daytime (mean sunlight intensity: 784.8 W m^{-2}), respectively. Due to the thermal resistance of the fully compressed SACNT aerogel, the temperature is slightly higher than the sample only with RC film. For the low mean ambient temperature of 20.8 °C at nighttime (Figure 5d), RCTR at "off" state can weaken the radiative cooling, resulting in a higher mean temperature (22.3 °C) than the ambient and the sample with RCTR at "on" state.

The practical thermal management of RCTR on real objects was further explored as shown in Figure 5e. One of the house models is directly exposed to the ambient, and the other three are covered by RC film, RCTR on "off" and "on" state, respectively. Figure 5f shows the house temperature changes recorded by K-type thermocouples under the mean solar irradiance of 847 W m^{-2} in the daytime. The house covered by RCTR at "on" state has a lower average temperature (36.3 °C) than the bare house (39.0 °C), indicating the practical cooling capability of RCTR. This phenomenon is also verified by the infrared images at 12:00 am (Figure 5g). When the cooling capacity is unacceptable at the cold environment during nighttime, RCTR can be tuned into "off" state to raise the house temperature by 1.1 °C than the bare house (Figure 5h). These experimental results highly demonstrate that the RCTR with a tunable heat dissipation capability has great potential in dynamic thermal management for space devices and buildings.

3. Conclusion

In summary, we present a continuously tunable and ultrawide-range thermal regulator based on the microstructure evolution of SACNT aerogel under compressive strain, which possesses an excellent practical performance in the thermal management of LIBs and house models. Experimental characterization and theoretical analysis of the thermal transport property of the SACNT aerogel demonstrate that the regulation of both thermal interfacial resistance and conductive pathways is vital for the ultrahigh thermal-conductivity change ratio (r≈43). The temperature and heat flux can be both tuned by the thermal regulator, showing more versatility than the conventional thermal switches with only "on" and "off" states. Profiting from this, the LIB with the dynamic thermal management based on the regulator exhibits a longer running time (250 s) in the optimal operation temperature range than the bare battery at the low temperature of 0 °C. Besides, the tunable heat radiation has been achieved by combining the thermal regulator with the RC film, which is proven to be able to actively lower the house temperature by 2.7 °C during daytime and raise it by 1.1 °C during nighttime compared with the bare house model. This efficient dynamic heat transfer control as well as the excellent mechanical flexibility and durability make this new type of thermal regulator promising for practical thermal management of batteries, buildings, spacecraft, etc.

4. Experimental Section

Materials: SACNT arrays used were grown on silicon wafers by a chemical vapor deposition (CVD) method.[25] Poly(vinylidene fluoride-co-hexafluoropropylene) (PVDF-HFP) and anhydrous ethanol were purchased from Shanghai Aladdin Biochemical Technology Co., Ltd. Graphene suspension was purchased from Beijing Meiston Technology Development Co., Ltd. N,N-Dimethylformamide (DMF) and tetrahydrofuran (THF) were purchased from Tianjin Kemat Chemical Technology Co., Ltd. Deionized water was obtained from the pure water machine. All purchased chemicals were of analytical purity. The lithium-ion battery (18650–3.6 V/2.0Ah) used in the battery thermal management experiment is fabricated by Far East Battery Co., Ltd, and the anode and cathode electrodes of this battery are graphite and lithium iron phosphate, respectively. More detailed battery information can be found in Table S2 (Supporting Information).

Fabrication of SACNT Aerogels: SACNT arrays (50 mg) were detached from the substrate and dispersed in ethanol solution (50 mL) by probe ultrasonication (power: 500 W) for 45 min. After the volume of this suspension was reduced to 10 mL by ethanol evaporation at 60 °C, deionized water (800 mL) was added to dilute the ethanol. Then, the suspension was placed in an oven at 90 °C to evaporate until the volume was reduced to 50 mL. Repeat this process three times to ensure that no ethanol remains. The suspension then underwent freeze-drying for ≈24 h. By changing the centration of the suspension, the aerogels with different density were obtained. Finally, the carbon deposition process in the atmosphere (200 sccm) with acetylene (100 sccm) at 800 °C for 20 min was followed to enhance the mechanical property of SACNT aerogels.

Fabrication of RC Films by the Electrospinning Method: PVDF-HFP particles were dissolved in a mixed solution of DMF and THF (volume ratio 7:3) and then the mixed solution was stirred for 1 h at 65 °C to obtain the electrospinning precursor (10 wt.%). The precursor was then added into a plastic syringe with a 19-gauge metal needle. RC film was collected on an aluminum foil-covered collector by electrospinning at a constant flow rate of 0.1 mL min^{-1} under a high voltage of 20 kV.

Characterization: The morphology of the samples was characterized by scanning electron microscopy (SEM, JEOL 7610F). XRD patterns were collected by an X-ray diffractometer (Smartlab 9 kW) at a scan rate of 5° min^{-1}. Raman spectrum was recorded by Raman spectrometer with a laser source of 532 nm (Thermo Electron, DXR Microscope). Thermal conductivity of the samples at different strains was measured by hot-disk method (Hot Disk, TPS2500S) according to the previous report.[30] The sample temperature was measured with k-type thermocouples, which were connected to a data collector (Fluke 2368A). Mechanical tests were carried out by an Instron 5848 microtester. The reflectivity and infrared emissivity were measured by UV–vis–NIR spectrophotometer (UV3600, Shimadzu Corporation) and FTIR spectrometer (Bruker INVENIO) with an integrating sphere (PIKE INTERRATIR), respectively. Infrared thermal images were taken with an IR camera (OPTRIS XI). Details about the experiment of the heat transfer regulation and battery thermal management can be found in Supporting Information.

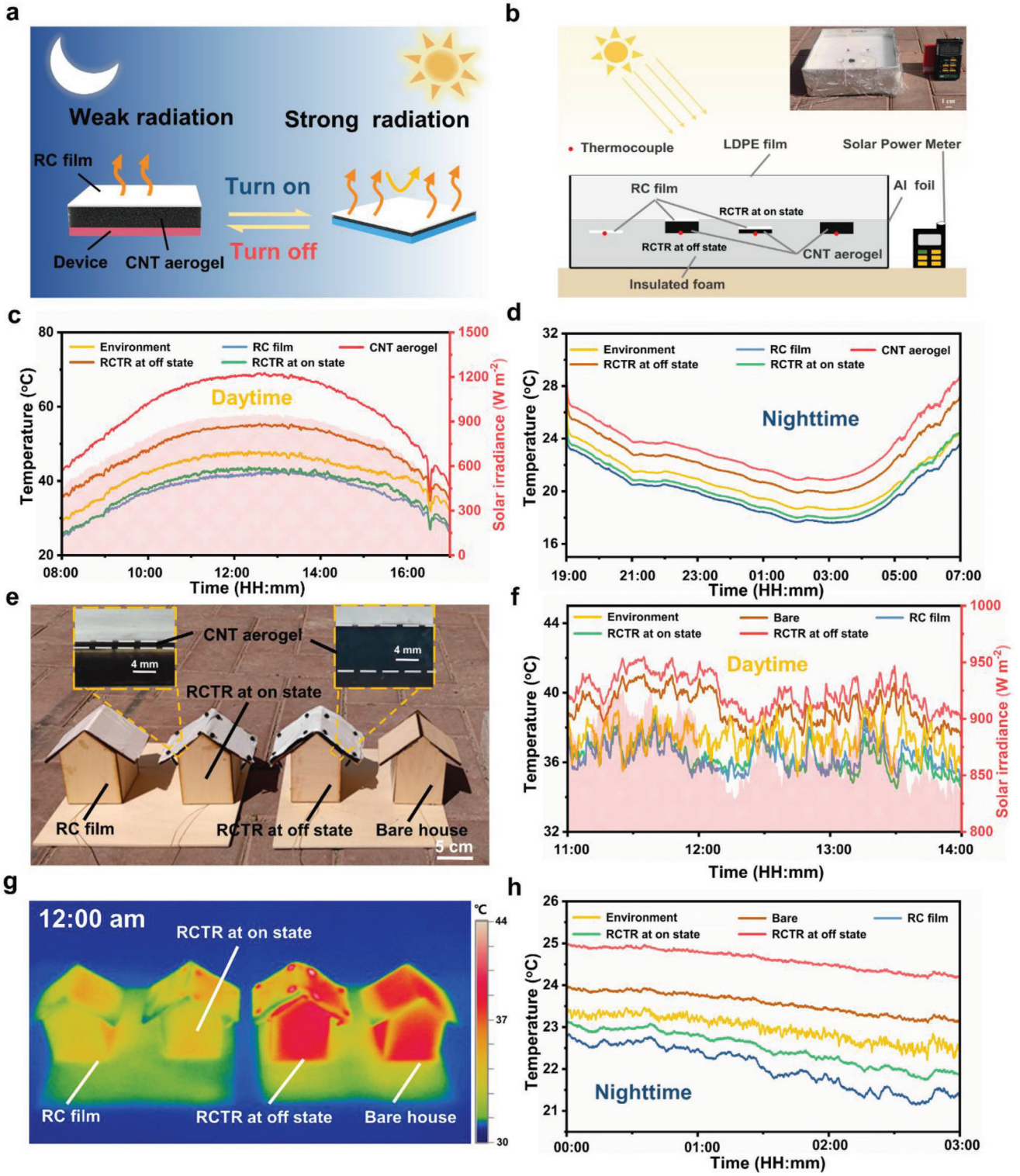

Figure 5. Dynamic thermal management of the house model. a,b) Schematic diagrams illustrating the working principle (a) and the experimental setup (b) of the radiative thermal management by combining the radiative cooling film and the thermal regulating SACNT aerogel (insert: photograph of the actual experimental setup). c,d)Temperature changes of the environment, the samples with RCTR at on and off state, the SACNT aerogel and the RC film during daytime (c) and nighttime (d). e) Photograph showing the experimental setup for the radiative thermal management of the house models, including one exposed, one covered with the RC film, and the other two equipped with the RCTR at on and off state (insert: optical images showing the cross-sectional view of the RCTR at the on (left) and off state (right). f) Temperature changes of the four house models during daytime (11:00–14:00). g) Infrared images of the four house models at 12:00 am. h) Temperature changes of the four house models during nighttime (00:00–3:00).

Supporting Information

Supporting Information is available from the Wiley Online Library or from the author.

Acknowledgements

This work was supported by the National Natural Science Foundation of China (52302041) and the Tianjin Municipal Education Commission Research Project (2022KJ094).

Conflict of Interest

The authors declare no conflict of interest.

Data Availability Statement

The data that support the findings of this study are available from the corresponding author upon reasonable request.

Keywords

CNT aerogel, dynamic thermal management, heat transfer control, lithium-ion battery, radiative cooling

Received: November 9, 2023
Revised: January 15, 2024
Published online: February 6, 2024

[1] A. Henry, R. Prasher, A. Majumdar, *Nat. Energy* **2020**, *5*, 635.
[2] G. Wehmeyer, T. Yabuki, C. Monachon, J. Wu, C. Dames, *Appl. Phys. Rev.* **2017**, *4*, 041304.
[3] A. Sood, F. Xiong, S. Chen, H. Wang, D. Selli, J. Zhang, C. J. McClellan, J. Sun, D. Donadio, Y. Cui, E. Pop, K. E. Goodson, *Nat. Commun.* **2018**, *9*, 4510.
[4] T. Du, Z. Xiong, L. Delgado, W. Liao, J. Peoples, R. Kantharaj, P. R. Chowdhury, A. Marconnet, X. Ruan, *Nat. Commun.* **2021**, *12*, 4915.
[5] S. Cheng, X. Guo, P. Tan, B. Yan, M. Lin, J. Cai, Y. Zhang, W. Cai, X. Zhang, *J. Mater. Chem. A* **2023**, *11*, 17779.
[6] S. Wang, T. Jiang, Y. Meng, R. Yang, G. Tan, Y. Long, *Science* **2021**, *374*, 1501.
[7] K. Tang, K. Dong, J. Li, M. P. Gordon, F. G. Reichertz, H. Kim, Y. Rho, Q. Wang, C.-Y. Lin, C. P. Grigoropoulos, A. Javey, J. J. Urban, J. Yao, R. Levinson, J. Wu, *Science* **2021**, *374*, 1504.
[8] I. Levchenko, K. Bazaka, T. Belmonte, M. Keidar, S. Xu, *Adv. Mater.* **2018**, *30*, 1802201.
[9] Y. Cui, H. Gong, Y. Wang, D. Li, H. Bai, *Adv. Mater.* **2018**, *30*, 1706807.
[10] S. D. Lubner, J. Choi, G. Wehmeyer, B. Waag, V. Mishra, H. Natesan, J. C. Bischof, C. Dames, *Rev. Sci. Instrum.* **2015**, *86*, 014905.
[11] C. Vélez, M. Khayet, J. M. Ortiz de Zárate, *Appl. Energy* **2015**, *143*, 383.
[12] S. Lee, K. Hippalgaonkar, F. Yang, J. Hong, C. Ko, J. Suh, K. Liu, K. Wang, J. J. Urban, X. Zhang, C. Dames, S. A. Hartnoll, O. Delaire, J. Wu, *Science* **2017**, *355*, 371.
[13] X. K. Zhang, J. Y. Li, J. C. Lin, P. Tong, M. Wang, X. L. Wang, H. Y. Tong, Y. S. Zhang, W. H. Song, Y. P. Sun, *Acta Mater.* **2021**, *208*, 116709.
[14] J. Zhou, Y. Wu, H. Kwon, Y. Li, X. Xiao, Y. Ye, Y. Ma, K. E. Goodson, H. Y. Hwang, Y. Cui, *Nano Lett.* **2022**, *22*, 5443.
[15] J. S. Kang, M. Ke, Y. Hu, *Nano Lett.* **2017**, *17*, 1431.
[16] P. Kim, L. Shi, A. Majumdar, P. L. McEuen, *Phys. Rev. Lett.* **2001**, *87*, 215502.
[17] K. J. Zhang, A. Yadav, K. H. Kim, Y. Oh, M. F. Islam, C. Uher, K. P. Pipe, *Adv. Mater.* **2013**, *25*, 2926.
[18] W. Yu, X. Zhao, P. Jiang, C. Liu, R. Yang, *Mater. Today Phys.* **2021**, *20*, 100447.
[19] P. Hu, J. Wang, P. Zhang, F. Wu, Y. Cheng, J. Wang, Z. Sun, *Adv. Mater.* **2023**, *35*, 2207638.
[20] X. Zhao, J. C. Wu, Z. Y. Zhao, Z. Z. He, J. D. Song, J. Y. Zhao, X. G. Liu, X. F. Sun, X. G. Li, *Appl. Phys. Lett.* **2016**, *108*, 242405.
[21] Y. Zeng, C.-L. Lo, S. Zhang, Z. Chen, A. Marconnet, *Carbon* **2020**, *158*, 63.
[22] F. Zhang, Y. Feng, M. Qin, L. Gao, Z. Li, F. Zhao, Z. Zhang, F. Lv, W. Feng, *Adv. Funct. Mater.* **2019**, *29*, 1901383.
[23] A. M. Marconnet, M. A. Panzer, K. E. Goodson, *Rev. Mod. Phys.* **2013**, *85*, 1295.
[24] W. Yu, C. Liu, S. Fan, *Nano Res.* **2021**, *14*, 2471.
[25] K. Jiang, J. Wang, Q. Li, L. Liu, C. Liu, S. Fan, *Adv. Mater.* **2011**, *23*, 1154.
[26] S. Luo, Y. Luo, H. Wu, M. Li, L. Yan, K. Jiang, L. Liu, Q. Li, S. Fan, J. Wang, *Adv. Mater.* **2017**, *29*, 1603549.
[27] W. Yu, G. Zhang, C. Liu, S. Fan, *ACS Nano* **2020**, *14*, 14091.
[28] W. Zhao, Y. Li, S. Wang, X. He, Y. Shang, Q. Peng, C. Wang, S. Du, X. Gui, Y. Yang, Q. Yuan, E. Shi, S. Wu, W. Xu, A. Cao, *Carbon* **2014**, *76*, 19.
[29] J. Shi, D. Han, Z. Li, L. Yang, S.-G. Lu, Z. Zhong, J. Chen, Q. M. Zhang, X. Qian, *Joule* **2019**, *3*, 1200.
[30] J. Chen, X. Gui, Z. Wang, Z. Li, R. Xiang, K. Wang, D. Wu, X. Xia, Y. Zhou, Q. Wang, Z. Tang, L. Chen, *ACS Appl. Mater. Interfaces* **2012**, *4*, 81.
[31] C. Li, Y. Ma, Z. Tian, *ACS Macro Lett.* **2018**, *7*, 53.
[32] J. Philip, P. D. Shima, B. Raj, *Appl. Phys. Lett.* **2007**, *91*, 203108.
[33] D.-W. Oh, C. Ko, S. Ramanathan, D. G. Cahill, *Appl. Phys. Lett.* **2010**, *96*, 151906.
[34] T. Zhang, T. Luo, *ACS Nano* **2013**, *7*, 7592.
[35] M. Qin, Y. Xu, R. Cao, W. Feng, L. Chen, *Adv. Funct. Mater.* **2018**, *28*, 1805053.
[36] S. Shen, A. Henry, J. Tong, R. Zheng, G. Chen, *Nat. Nanotechnol.* **2010**, *5*, 251.
[37] X. Liu, P. Li, J. Chen, P. Jiang, Y.-W. Mai, X. Huang, *Sci. Bull.* **2022**, *67*, 1991.
[38] Y. Zeng, B. Zhang, Y. Fu, F. Shen, Q. Zheng, D. Chalise, R. Miao, S. Kaur, S. D. Lubner, M. C. Tucker, V. Battaglia, C. Dames, R. S. Prasher, *Nat. Commun.* **2023**, *14*, 3229.
[39] J. Luo, D. Zou, Y. Wang, S. Wang, L. Huang, *Chem. Eng. J.* **2022**, *430*, 132741.
[40] J. Kim, J. Oh, H. Lee, *Appl. Therm. Eng.* **2019**, *149*, 192.
[41] M. Hao, J. Li, S. Park, S. Moura, C. Dames, *Nat. Energy* **2018**, *3*, 899.
[42] L. Li, B. Fang, D. Ren, L. Fu, Y. Zhou, C. Yang, F. Zhang, X. Feng, L. Wang, X. He, P. Qi, Y. Liu, C. Jia, S. Zhao, F. Xu, X. Wei, H. Wu, *ACS Nano* **2022**, *16*, 10729.
[43] Y. Zhai, Y. Ma, S. N. David, D. Zhao, R. Lou, G. Tan, R. Yang, X. Yin, *Science* **2017**, *355*, 1062.
[44] T. Li, Y. Zhai, S. He, W. Gan, Z. Wei, M. Heidarinejad, D. Dalgo, R. Mi, X. Zhao, J. Song, J. Dai, C. Chen, A. Aili, A. Vellore, A. Martini, R. Yang, J. Srebric, X. Yin, L. Hu, *Science* **2019**, *364*, 760.

